Advanced Intelligent Systems

ADVANCED INTELLIGENT SYSTEMS Open Access

www.advintellsyst.com

RESEARCH ARTICLE OPEN ACCESS

Physics-Informed Machine Learning for Predicting Phases and Density of Al_2O_3–TiB_2 Composites Synthesized via Laser Ignition From the Al–TiO_2–B_2O_3–H_3BO_3 Reactive System

Evangelos Daskalakis | Geeta Sharma | Sarathkumar Loganathan | Andrew Scott | Animesh Jha

School of Chemical and Process Engineering, University of Leeds, Leeds, UK

Correspondence: Evangelos Daskalakis (Evangelos.Daskalakis@outlook.com)

Received: 25 March 2026 | **Revised:** 18 September 2026 | **Accepted:** 23 September 2026

Keywords: laser ignition chemical synthesis | ML prediction model | physics-informed machine learning | self-propagating high-temperature synthesis TiB_2–Al_2O_3

ABSTRACT

Predicting phase transformation in multicomponent, highly exothermic reactive systems remains a challenge. Variations in stoichiometry and processing parameters affect the phase purity and density of in situ manufactured composites. This work presents a novel physics-informed machine learning (PIML) model to predict the composition and bulk density of Al_2O_3–TiB_2 composites synthesized through furnace SHS and laser ignition chemical synthesis (LIChemS) from the Al–TiO_2–B_2O_3–H_3BO_3 reactive system. The PIML model integrates physics rules across a multioutput mass-fraction model (Model 1—V1, V2, V3), a bulk density model (Model 2), and a compositional–topological interpretation model (Model 3). Model 1 (V1, V2) achieved hold-out testing R^2 of 0.994, whereas the unconstrained V3 produced nonphysical outputs, including negative mass fractions. LIChemS composites yielded $mAl_2O_3 = 0.69$ and $mTiB_2 = 0.22$ (purity = 0.91), with the model deviating by 3 wt%. Model 2 achieved test $R^2 = 0.927$, with the ML and experimental densities being 3.68 and 3.71 g/cc, respectively. Pareto optimization identified optimal processing windows near ignition thresholds, targeting purity > 0.85 and bulk density > 3.5 g/cc. Ternary and tetrahedral mapping demonstrated that LIChemS yielded Al_2O_3–TiB_2 outputs. The developed PIML model provides a time- and material-efficient approach to optimizing reactive system outputs in industrial settings.

1 | Introduction

Self-propagating high-temperature synthesis (SHS) describes highly exothermic, energy-efficient reactions that enable the in situ synthesis of ultra-hard ceramic composites such as Al_2O_3–TiB_2 [1–3]. During SHS, ceramic oxides are reduced by metal agents, in an inert or vacuum atmosphere, as the products are of redox nature in the absence of atmospheric oxygen [4]. The processing of the reactants and the ignition parameters during conventional SHS and LIChemS directly impact the phase transformation and bulk density of the produced ceramic composites [5–8]. The Al_2O_3–TiB_2 composites present high hardness (~1950 HV), chemical inertness, and thermal stability, making them suitable for wear-resistant coatings, cutting tools, and structural components in extreme environments [9–11].

The reaction stoichiometry in the Al–TiO_2–B_2O_3-H_3BO_3 system directly impacts the composition and bulk density outputs of the synthesized composites [12–14]. The B_2O_3 phase absorbs atmospheric water and converts into H_3BO_3 [10]. Upon the decomposition of boric acid (H_3BO_3), only 56 wt% of H_3BO_3 converts to B_2O_3. This partial conversion can compromise the stoichiometry

This is an open access article under the terms of the Creative Commons Attribution License, which permits use, distribution and reproduction in any medium, provided the original work is properly cited.

© 2026 The Author(s). *Advanced Intelligent Systems* published by Wiley-VCH GmbH.

of B_2O_3 [10, 15]. Rapid degassing of water and impurities during SHS induce porosity in the composites. Heat treating and milling the reactants can reduce the ignition threshold of SHS and improve the yield of the wanted products [10, 14].

Any deviations from optimized processing, as identified by Daskalakis et al., in the Al–TiO_2–B_2O_3–H_3BO_3 system, could lead to the formation of side product phases such as Ti–O or Al–B–O [16–18]. Experimental trial-and-error can be time-consuming, resource-intensive, and prone to human error, which limits the efficiency of the optimization process, especially in an industrial scale setting. Simulation and ML-driven approaches can provide a more systematic and cost-effective pathway to optimization.

Conventional modeling does not examine nonequilibrium interactions, such as those occurring during LIChemS in the Al–TiO_2–B_2O_3 system [19]. CALPHAD can model the thermodynamic properties and phase stability of multicomponent alloy and ceramic systems under idealized conditions but does not account for phase transformation during rapid heating and SHS originating from localized energy input such as LIChemS [20–22]. Kinetic and SHS-specific models provide a more mechanistic view of the reaction-front propagation, describing physical and chemical processes during SHS such as heat generation and conduction and reaction kinetics, but they require extensive calibration, which limits their applications [23–25]. These approaches, however, do not consider dehydration and decomposition of reactants, milling, furnace- or laser-induced SHS, or ignition thresholds in a single framework.

Data-driven machine learning (ML) has emerged as a powerful tool for predicting phases and optimizing manufacturing processes [26–28]. However, purely statistical models applied to the Al–TiO_2–B_2O_3 reactive system could yield physically not permissible outputs, such as negative mass fractions and mass imbalance between reactants and products [29–31]. Especially in reactive systems, where the synthesis outcomes are constrained by reaction stoichiometry and thermodynamics, the experimental data can be limited.

Machine learning models can understand complex trends but require the application of constraint enforcements to ensure that they provide valid outputs, especially in threshold-driven reactions [32–35]. Physics-informed and physics-constrained machine learning approaches combine the predictive flexibility of ML models and the physical constraints describing exothermic reactions [36–38]. The PIML model integrates conservation laws and constraints regarding processing parameters and reaction stoichiometry and interactive ML, where parameter input could also be provided by the ML model user.

In this work, we develop a novel interactive physics-informed machine learning (PIML) model for predicting the phase purity and bulk density of Al_2O_3–TiB_2 composites synthesized through furnace SHS or LIChemS from the Al–TiO_2–B_2O_3–H_3BO_3–H_2O system. The model incorporates physics constraints to capture: (i) H_3BO_3 dehydration, (ii) effective B_2O_3 availability in the system, (iii) stoichiometric deviation, (iv) milling enhanced ignition, (v) ignition thresholds for laser and furnace, (vi) ignition-dependent Al–B–O and Ti–O side phase formation, and (vii) rule of mixture baseline densification factor. All ML predictive outputs were subjected to physics constraints to ensure permissible outputs such as non-negative phase fractions and mass conservation. Using 3800 composition-processing channels, we demonstrated high predictive accuracy for stoichiometric and nonstoichiometric reactions. The model developed in this work could emerge as a predictive tool for the design and optimization of multicomponent reactive systems in an industrial setting.

2 | Materials and Methods

2.1 | Experimental Dataset and Inputs

The physics-informed machine learning (PIML) model developed in this work consisted of 3 individual components, Model 1, Model 2, and Model 3, Supporting Information S2.1. Model 1 predicted the composition of the products deriving from the highly exothermic aluminothermic reduction of titanium dioxide and boron oxide (Equation (I)).

$$\frac{10}{3}\,\mathrm{Al} + \mathrm{TiO_2} + \mathrm{B_2O_3} \rightarrow \frac{5}{3}\,\mathrm{Al_2O_3} + \mathrm{TiB_2} \qquad \text{(I)}$$

Model 2 then predicted the bulk density of the composites, while Model 3 provided a mechanistic visualization of the products deriving from the reaction pathways.

2.2 | Model 1—Mass Fraction Models

The reaction stoichiometry of Equation (I), as explained by Daskalakis et al. [10, 14], defined the target stoichiometric mass fraction of 0.375 Al–0.334 TiO_2–0.291 B_2O_3. The dataset primarily explored the impact of 8 processing parameters on three compositional variations of the (Al–TiO_2–B_2O_3) reactive system (Table 1). Option 1 corresponded to the stoichiometric "dry" composition of

TABLE 1 | A summary of the reactive mixtures.

Options	Chemistry	Status
1	(0.375 Al–0.334 TiO_2–0.291 B_2O_3)	Stoichiometric ignition
2	(0.375 Al–0.334 TiO_2–0.221 B_2O_3–0.070 H_3BO_3)	Nonstoichiometric ignition
3	(0.350 Al–0.312 TiO_2–0.234 B_2O_3–0.074 H_3BO_3–0.030 H_2O)	Process-dependent stoichiometric ignition
4	Customization	

Equation (I), while Option 2 referred to a nonstoichiometric composition containing a mixture of B_2O_3–H_3BO_3 [10]. Option 3 described a process-dependent stoichiometric composition accounting for H_3BO_3 decomposition and H_2O evaporation under specific processing conditions. Option 4 allowed for user-defined reactant compositional input. All mass fractions added up to 1.

The dataset comprised 3800 rows (channels), each containing five reactant inputs (R1–R5), eight processing parameters, and 12 output phase fractions (Table 2).

The dataset was split into 12 subsystems, including single-reactant baselines (Al, TiO_2, B_2O_3, H_3BO_3, and H_2O), binary and intermediate systems (Al–B_2O_3, Al–TiO_2, Al–B_2O_3–H_3BO_3), and multicomponent reactive systems processed by furnace SHS and LIChemS (Table 3). The single-reactant and binary subsystems taught the model about regions where no product phases form, whereas the Al–TiO_2–B_2O_3–H_3BO_3 reactive system contained Al_2O_3–TiB_2 products.

The phase fractions in each channel were obtained from (i) experimental measurements and quantitative phase fractions (XRD/Rietveld), as described by Daskalakis et al. [10, 14] (≈8% of channels); (ii) the literature [10, 14, 39–50] (≈79%); and (iii) systematic rule-based augmentation of the experimental and literature channels using the deterministic physics preprocessing of Section 2.3 (≈13%). The bulk-density values used to train Model 2 (Section 2.6) were obtained by experimental measurement (helium pycnometry, Section 2.12) on 192 pellets across three reactant packages. Not all 12 output phases were populated in every channel, as the product phases cannot form in single-reactant and binary-system channels. The Al_2O_3–TiB_2 composite was produced in multicomponent reactive channels (Figure 1).

Model 1 predicted a 12 phase mass-fraction output including unreacted phases (UR1–UR5), target products (P1: Al_2O_3; P2: TiB_2), and side phases (SP1–SP5) (Table 2). All predicted compositions were normalized to satisfy mass conservation, and water (UR5) was excluded during postignition solid-phase renormalization.

TABLE 2 | Nomenclature of the model output phases.

Unreacted reactants	Product phases	Side-product phases
UR1=Al	P1=Al_2O_3	SP1=Ti_2O_3
UR2=TiO_2	P2=TiB_2	SP2=$TiAl_3$
UR3=B_2O_3		SP3=Al_5BO_9
UR4=H_3BO_3		SP4=$Al_{18}B_4O_{33}$
UR5= H_2O		SP5=$TiBO_3$

2.3 | Physics-Informed Feature Engineering

To improve the predictive accuracy of the model, physics features were integrated. The physics features were computed using a deterministic preprocessing function applied to each input row. The key physics features are summarized in Table 4.

Mechanical milling was implemented as a binary modifier, reducing the ignition threshold and increasing reaction probability. Thermal regimes for the (Al–TiO_2–B_2O_3–H_3BO_3–H_2O) system were defined based on the literature [10] (Table 5).

In the 0–100 °C regime, no change was observed, while between 100 and 180 °C, water evaporated. Water drying was modeled with a first-order moisture removal law at the applied drying temperature (Equations (1) and (2)). The (k_d) was assigned experimentally. The measured drying conditions within 1 h and the measured fraction of water removed from the samples are included in the Supporting Information S2.2.

$$\frac{dm_w}{dt} = -k_d(m_w - m_w,\infty) \tag{1}$$

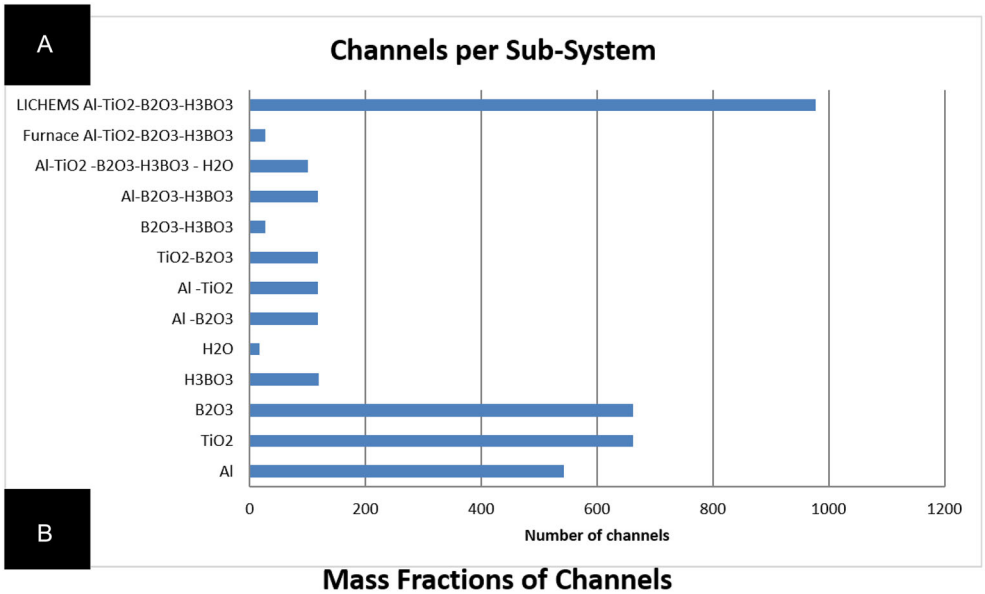
And

$$m_w(t) = m_w,\infty + \left(m_{w,0} - m_{w,\infty}\right)e^{-k_d t} \tag{2}$$

where $m_{w,0}$ = initial water, $m_{w,\infty}$ = residual water, and k_d = drying rate constant (1/s).

TABLE 3 | Dataset composition by chemical subsystem.

Subsystem	Channels	Role	References
Al, TiO_2, B_2O_3, H_3BO_3, H_2O	2004	Baseline (no reaction)	No reaction
Al–B_2O_3, Al–TiO_2, TiO_2–B_2O_3, B_2O_3–H_3BO_3	381	Binary subsystems	No reaction, experimental literature: [10, 14, 39–50]
Al–B_2O_3–H_3BO_3, Al–TiO_2–B_2O_3–H_3BO_3–H_2O	218	Intermediate	No reaction, experimental literature: [10, 14, 39–50]
Furnace SHS (Al–TiO_2–B_2O_3–H_3BO_3)	27	Reactive	Experimental
LIChemS (Al–TiO_2–B_2O_3–H_3BO_3)	978	Reactive	No reaction, experimental literature: [10, 14, 39–50] Augmented
Density measurements	192	Bulk density	Experimental
Total	3800		



Sub-system	UR1	UR2	UR3	UR4	UR5	P1	P2	SP1	SP2	SP3	SP4	SP5
Al	1.00	0.00	0.00	0.00	0.00	0.00	0.00	0.00	0.00	0.00	0.00	0.00
TiO2	0.00	1.00	0.00	0.00	0.00	0.00	0.00	0.00	0.00	0.00	0.00	0.00
B2O3	0.00	0.00	1.00	0.00	0.00	0.00	0.00	0.00	0.00	0.00	0.00	0.00
H3BO3	0.00	0.00	0.48	0.68	0.48	0.00	0.00	0.00	0.00	0.00	0.00	0.00
H2O	0.00	0.00	0.00	0.00	1.00	0.00	0.00	0.00	0.00	0.00	0.00	0.00
Al -B2O3	0.86	0.00	0.80	0.00	0.00	0.56	0.00	0.00	0.00	0.73	0.24	0.00
Al -TiO2	0.70	0.73	0.00	0.00	0.00	0.51	0.00	0.00	0.51	0.00	0.00	0.00
TiO2-B2O3	1.00	1.00	0.00	0.00	0.00	0.00	0.00	0.00	0.00	0.00	0.00	0.00
B2O3-H3BO3	0.00	0.00	1.00	0.33	0.00	0.00	0.00	0.00	0.00	0.00	0.00	0.00
Al-B2O3-H3BO3	0.99	0.00	0.99	0.13	0.99	0.75	0.00	0.00	0.00	0.75	0.75	0.00
Al-TiO2 -B2O3-H3BO3 - H2O	0.84	0.84	0.84	0.32	0.92	0.16	0.16	0.15	0.00	0.28	0.31	0.00
Furnace Al-TiO2-B2O3-H3BO3	0.70	0.70	0.70	0.15	0.00	0.30	0.30	0.00	0.22	0.37	0.30	0.15
LICHEMS Al-TiO2-B2O3-H3BO3	0.00	0.00	0.00	0.00	0.00	1.00	1.00	1.00	0.94	0.95	0.19	0.00

FIGURE 1 | (A) Composition of the training library by sub-system. (B) Mass fraction of channels in which each output phase is populated.

TABLE 4 | The key physics features that were integrated in the PIML model.

No	Physics features
1	Effect of milling on the ignition threshold
2	Dehydration of H_3BO_3 (R4) converting into effective B_2O_3 (R3) and H_2O (R5)
3	Temperature-regime indicators
4	Ignition indicators for furnace and laser based dynamic ignitions
5	Stoichiometric descriptors
6	Products descriptors
7	Side product favoritism depending on laser or furnace ignition

TABLE 5 | The thermal regimes defined in the Al–TiO_2–B_2O_3–H_3BO_3–H_2O system.

Temperature range, °C	Physical significance
0–100	No change
100–180	Water removal
180–450	H_3BO_3 decomposition and water removal
450–660	Melting of B_2O_3 molten
≥660	Al melting
≥936	TiB_2 formation onset
≥1050	Secondary aluminoborate phase

In the 180–450 °C regime, boric acid (R4 = H_3BO_3) decomposed according to Equation (II).

$$2\,H_3BO_3 = B_2O_3 + 3H_2O \quad \text{(II)}$$

Complete dehydration of H_3BO_3 yielded 0.563 B_2O_3–0.437 H_2O. Partial dehydration was permitted below 180 °C, and full dehydration of the reactants was enforced above 200 °C. The evaporated water from both moisture (R5) and H_3BO_3 (R4) decomposition was expressed as an output phase UR5. The effective B_2O_3 was defined by Equation (3):

$$m_{B_2O_{3\text{eff}}} = m_{B_2O_3} + 0.563 * m_{H_3BO_{3\text{Decomp}}} \quad (3)$$

Between 450 and 660 °C, B_2O_3 (R3) was considered "molten B_2O_3," and capable of interacting with the Al_2O_3 oxide coating on the surface of the Al particles, forming aluminoborate phases

(Al_2O_3–B_2O_3) (Equation (III)).

$$5Al_2O_3 + B_2O_3 = 2Al_5BO_9 \quad \text{(III)}$$

Between 660 and 938 °C, molten Al reduced B_2O_3 according to Equation (IV).

$$2Al + B_2O_3 = Al_2O_3 + 2B \quad \text{(IV)}$$

At 936 °C, the onset of TiB_2 formation marked exothermic reaction ignition. The reaction ignition was governed by two parallel mechanisms involving (i) furnace ignition and (ii) laser ignition described by Equations (4)–(6).

$$\begin{aligned} T_{ign} &= 936 - 50°C \text{ for milled reactants} \\ T_{ign} &= 936 + 200°C \text{ for un} - \text{milled reactants} \end{aligned} \quad (4)$$

Furnace ignition occurred when:

$$T_{sinter} \geq T_{ign} \quad (5)$$

Laser ignition occurred when:

$$I_{laser} \geq 0.94\,W/mm^2 \quad (6)$$

The Al_2O_3 phase was allowed to form under subignition conditions; however, the TiB_2 phase was allowed only if at least one ignition pathway was activated. Secondary aluminoborate formation was allowed above 1050 °C, as $Al_{18}B_4O_{33}$ formed over Al_2O_3. Laser ignition favored the formation of the Ti_2O_3 phase over Al–B–O phases, while furnace ignition favored the opposite effect.

2.4 | Postprediction Constraint Enforcement

The stoichiometry of the reactants was evaluated and normalized for Al, TiO_2, and effective B_2O_3, using Equation (7).

$$x_i = \frac{m_i}{m_{Al} + m_{TiO_2} + m^{eff}_{B_2O_3}} \quad (7)$$

The L1-norm deviation metric was computed according to Equation (8).

$$\Delta_{stoich} = |x_{Al} - 0.375| + |x_{TiO_2} - 0.334| + |x_{B_2O_3} - 0.291| \quad (8)$$

For ($\Delta_{stoich} \leq 0.03$), the mixtures were classified as stoichiometric, accounting for scaling errors in reactants and partial decomposition of H_3BO_3. Following the ML prediction, all outputs were clipped to non-negative values and renormalized to satisfy Equation (9).

$$\sum_i fi = 1 \quad (9)$$

A rule-based enforcement step was applied following ML predictions, available in the Supporting Information S2.1. This rule-based enforcement ensured that all predictions remained physically permissible, particularly in extrapolative regions where the experimental dataset was not available. The rule-based enforcement is described below:

I. Ignition indicators: Furnace ($T_{sinter} \geq T_{ig}$) and $I_{laser} \geq 0.94\,W/mm^2$
II. Stoichiometric class: Classify stoichiometric if $\Delta_{stoich} \leq 0.03$
III. Predict phase fractions using the ML regressor.
IV. Enforce physical permissible results, which includes clipping negative outputs to 0 and renormalizing so that ($\sum_i fi = 1$).
V. Ignition gating: If no ignition, P2(TiB_2) = 0, but allow P1(Al_2O_3) within the defined subignition window.
VI. Stoichiometric ignition: Suppress unreacted fractions and renormalize mass across P1 and P2
VII. Nonstoichiometric ignition: Allocate the residual mass fraction after P1, P2, and UR5 into side-products (70%) and unreacted species (30%), distributed according to the normalized Al–TiO_2–B_2O_3 ratios.
VIII. Ignition-specific bias of side products: Laser ignition increases Ti–O preference (SP1) relative to Al–B–O phases; furnace ignition increases Al–B–O preference (SP3/SP4) relative to SP1.

2.5 | Model 1: Mass Fractions—Version 1, Version 2, and Version 3

Three version of Model 1 were evaluated to predict the composition of Al_2O_3–TiB_2 composites synthesized through furnace SHS and LIChemS following the application of 8 processing parameters on the Al–TiO_2–B_2O_3–H_3BO_3–H_2O reactive system. Version 1 employed a supervised multioutput regression model (Random Forest or Gradient Boosting) to predict the full 12-component mass-fraction vector (UR1–UR5, P1–P2, SP1–SP5) (Table 2), followed by deterministic physics preprocessing and postprediction constraint enforcement. The prediction of "purity" = P1 + P2 was a derived metric after the ML prediction and not a supervised learning target. Version 2 retained the V1 mass-fraction pipeline and additionally trained a single-output Random Forest model to predict purity (P1 + P2) directly, with hyperparameters tuned by a randomized search under Shuffle Split cross-validation. V2 reduced variance and mitigated overfitting for "purity" = P1 + P2. In V3, all deterministic physics parameters were disabled, enabling an ML-only prediction mode. The disabled physics parameters of version 3 excluded: (i) dehydration calculations, (ii) H_3BO_3 decomposition, (iii) ignition thresholds, (iv) stoichiometric metrics, (v) mass normalization, and (vi) any postprediction constraints. The model was trained using the same experimental dataset and machine learning architecture as Version 1 Supporting Information S2.3.

2.6 | Model 2—Bulk Density Prediction Model

ML prediction of the bulk density of the composites was defined by Equation (10).

$$p_{Dataset} = ML(R1, R2, R3, R4, R5, \text{processing}) \quad (10)$$

A physics-based baseline density was also computed from the predicted phase mass fractions using the rule of mixtures

(pRoM) (Equation (11)). Water (UR5) was excluded from the density calculations.

$$p_{\mathrm{RoM}} = \frac{1}{\sum_i \left(\frac{w_i}{p_i}\right)} \tag{11}$$

where (w_i) is the mass fraction of phase and (p_i) is the bulk density the phase.

A densification factor (f) was introduced from the ML density (p_{dataset}) and the rule of mixtures density (p_{RoM}) (Equation (12)).

$$f = \frac{p_{\mathrm{Dataset}}}{p_{\mathrm{RoM}}} \tag{12}$$

Equation (13) then provided the final bulk density prediction from the physics-informed model.

$$p_{\mathrm{pred}} = \mathrm{clip}\left(f_{\mathrm{pred}}, f_{\mathrm{min}}, f_{\mathrm{max}}\right) * p_{\mathrm{RoM}} \tag{13}$$

Equation (14) then provided a blended estimate of the density.

$$p_{\mathrm{blend}} = (1-\lambda)\, p_{\mathrm{ML}} + \lambda\, p_{\mathrm{RoM}}, \quad 0 \le \lambda \le 1 \tag{14}$$

Two error metrics were reported on the hold-out test: (i) MAE (mean absolute error) in g/cc (Equation (15)) and (ii) RMSE (root mean squared error) in g/cc (Equation (16)).

$$\mathrm{MAE} = \frac{1}{N}\sum |y - \widehat{y}| \tag{15}$$

and

$$\mathrm{RMSE} = \sqrt{\frac{1}{N}\sum (y-\widehat{y})^2} \tag{16}$$

2.7 | Machine-Learning Models and Evaluation

The dataset comprised approximately 3800 unique composition–processing combinations (channels), obtained from experimental measurements (8%), the literature (79%), and systematic augmentation (13%), through rule-based combinations. Random forest and gradient-boosting regressors were evaluated for phase prediction using an 80/20 hold-out split and 5-fold cross-validation. Model selection was based on the R^2 of purity (P1 + P2). Density was modeled using a random-forest regressor and evaluated using hold-out R^2, MAE, and RMSE. All models were implemented in Python (scikit-learn). A detailed description of the machine learning parameters for each model is listed in the Supporting Information S2.4.

2.8 | Processing-2D Heat Maps

To visualize process–property relationships, 2D heat maps were generated. For Model 1—V1, V2, and V3, the heat maps demonstrated the purity of the wanted products of Al_2O_3 and TiB_2 (P1 + P2) and individual product fractions (P1) and (P2) in regard to convective furnace heating (°C) and laser intensity (W/mm^2) processing parameters, with the furnace and laser ignition thresholds displayed in the map. For bulk density, maps displayed the predicted density as a function of different processing parameters.

2.9 | Case Studies

Two case studies were carried out between the (i) physics-informed ML models (V1, V2) and pure ML model (V3) and (ii) physics-informed ML models and experimental data. Table 6 describes the processing parameters used for the first case study. The predictive models were tested on the predefined (i) stoichiometric, (ii) nonstoichiometric, and (iii) conditional stoichiometric compositions of Table 1.

For the second case study, the processing parameters selected are described in Table 7. The accuracies of Model 1—V1 and V2 and Model 2 were tested against LIChemS products from nonstoichiometric composition (Option2—Table 1).

TABLE 6 | The processing parameters for carrying out the first case study.

Parameters	Ignition parameters	No ignition parameters
Milling	(0 = No, 1 = Yes): 1	(0 = No, 1 = Yes): 1
Powder drying temperature, °C/1 h	300	300
Compaction pressure, MPa	300	300
Pellet sintering temperature, °C/1 h	500	500
Furnace sintering time, h	1	1
Laser sintering, W/mm^2	0.94	0.44
Sintering time, min	5	5
LIChemS laser intensity, W/mm^2	0.94	0.44

TABLE 7 | The processing parameters for carrying out the second case study.

Parameters	ML and experimental data
Milling	(0 = No, 1 = Yes): 1
Powder drying temperature, °C/1 h	200
Compaction pressure, MPa	250
Pellet sintering temperature, °C/1 h	300
Furnace sintering time, h	2
Laser sintering, W/mm^2	0.66
Sintering time, min	1
LIChemS laser intensity, W/mm^2	0.94

2.10 | Multiobjective Optimization and Pareto Analysis

Pareto analysis aimed to identify the optimal processing windows for simultaneous improvement of the phase purity (P1 + P2) and bulk density of the Al_2O_3–TiB_2 composite while reducing the mass fraction of the side product (SP1–SP5). A total of 800 processing combinations were randomly sampled. The processing parameter bounds selected are displayed in Table 8.

Mass fractions were predicted using Model 1—V1, V2 (physics-informed), and V3 (pure ML), while bulk density was predicted using Model 2. Nondominated sorting was performed to identify Pareto-optimal solutions.

2.11 | Model 3—Data-Driven Reaction Mapping and Product Space Modeling

A stoichiometric–topological mapping workflow was implemented in Python (Supporting Information S2.1) to (i) visualize a data-driven frequency-weighted phase dominance map, (ii) depict where solid products lay within the Al–Ti–B compositional space following SHS, and (iii) provide a mechanistic tetrahedral map of the reaction pathway topology. For the frequency-weighted phase dominance map, reactant compositions were converted to elemental fractions (Al–Ti–B–O) and were projected into tetrahedral barycentric coordinates, where each data point was assigned a dominant output phase by argmax of predicted phase fractions. Then, the predicted products were projected into the Ti–B–Al ternary plane by reducing oxygen-containing phases to metallic constituents and renormalizing atomic fractions. The reaction topology map was generated by linking stoichiometric centroids of reactants and products using a predefined reaction library (Equations (15) –(24)),and a more detailed description of Model 3 is available in Supporting Information S2.5.

A tetrahedral coordinate system was defined using the elemental vertices of (i) Al, (ii) B, (iii) Ti, and (iv) O. The atomic fractions for each phase were calculated (Equation (17)) and were mapped into a 3D barycentric tetrahedral coordinate system.

$$x_i = \frac{n_i}{n_{Al} + n_B + n_{Ti} + n_O} \tag{17}$$

Reaction arrows were plotted between the stoichiometric centroids of reactants and products, producing a mechanistic topology map.

TABLE 8 | Pareto analysis processing parameters bound conditions.

Parameters	Values
Powder drying temperature	0–400 °C
Compaction pressure	0–500 MPa
Pellet sintering temperature	0–1100 °C
Furnace sintering time	0–5 h
LIChemS laser intensity	0–2 W/mm^2
Laser exposure time	0–10 min

2.12 | Experimental Setup and Engineering Characterization

The model outputs were compared with the published literature and experimental findings from this research. The experimental setup was the same as described by Daskalakis et al. [14]. The reactants were ball-milled in a RETSCH MM200 at 30 Hz. The ball–to–mass ratio was 9:5 (1.8), corresponding to a 9g alumina ball and 5g reactant powder. Powder and pellet drying and sintering, respectively, took place in a CARBOLITE Heating Laboratory Chamber Furnace. A hydraulic mechanical press performed the cold pressing. The samples were pressed for 5 min to form cylindrical pellets of 10-mm diameter and 3-mm thickness. Laser processing and LIChemS were performed by an Amtron fiber-optic-integrated quasi-CW diode laser (976 nm), with a maximum output power of 30 W. LIChemS took place inside a stainless-steel vessel (100 mm^3) in an argon atmosphere. The flowrate was set to 1 L/min. The identification and quantification of the phases in the composites ($N = 3$) were performed by X-ray diffraction (XRD) (Bruker D8), with monochromatic CuKα radiation ($\lambda = 0.154$ nm) and a 2θ range of 10°–80° and High Score Plus software. Phase quantification was performed using Rietveld analysis with HighScore Plus software. The bulk density measurements were performed by a ThermoFisher Scientific Helium-Pycnomatic was used at 20 C, for 20 cc sample volume, while the average of 10 runs was collected.

2.13 | Overview

An overview of the experimental plan isdepicted in Figure 2.

3 | Results

3.1 | Hold-Out Accuracy, 5-Fold Cross Validation, and Learning Curves

The PIML model developed for the (Al–TiO_2–B_2O_3) system demonstrated high predictive performance for both mass fraction and bulk density of the composites.

In Figure 3 and Table 9 (V1), the Random Forest regressor exhibited a hold-out testing R^2 of 0.994 with a MAE of ±0.0035, while the Gradient Boosting regressor exhibited a testing R^2 of 0.993 with a MAE of ±0.0035. Fivefold cross-validation yielded $R^2 = 0.989 \pm 0.002$ for the Random Forest regressor and 0.993 ± 0.001 for Gradient Boosting, confirming stable generalization. Phase purity (P1 + P2) was not selected as the supervised learning target by the model, but instead as a derived quantity, equally treated along with the other 10 phases. Errors during predictions may have been amplified during the normalization of the predicted mass fractions and the application of physics enforcement rules, compromising purity prediction.

In Version 2, phase purity (P1 + P2) was treated as a supervised target, predicted by a single-output Random Forest regressor. The hold-out test R^2 was slightly reduced to 0.993.

Version 3 served as a control case, where all physics-based preprocessing constraint rules were disabled. Version 3 presented

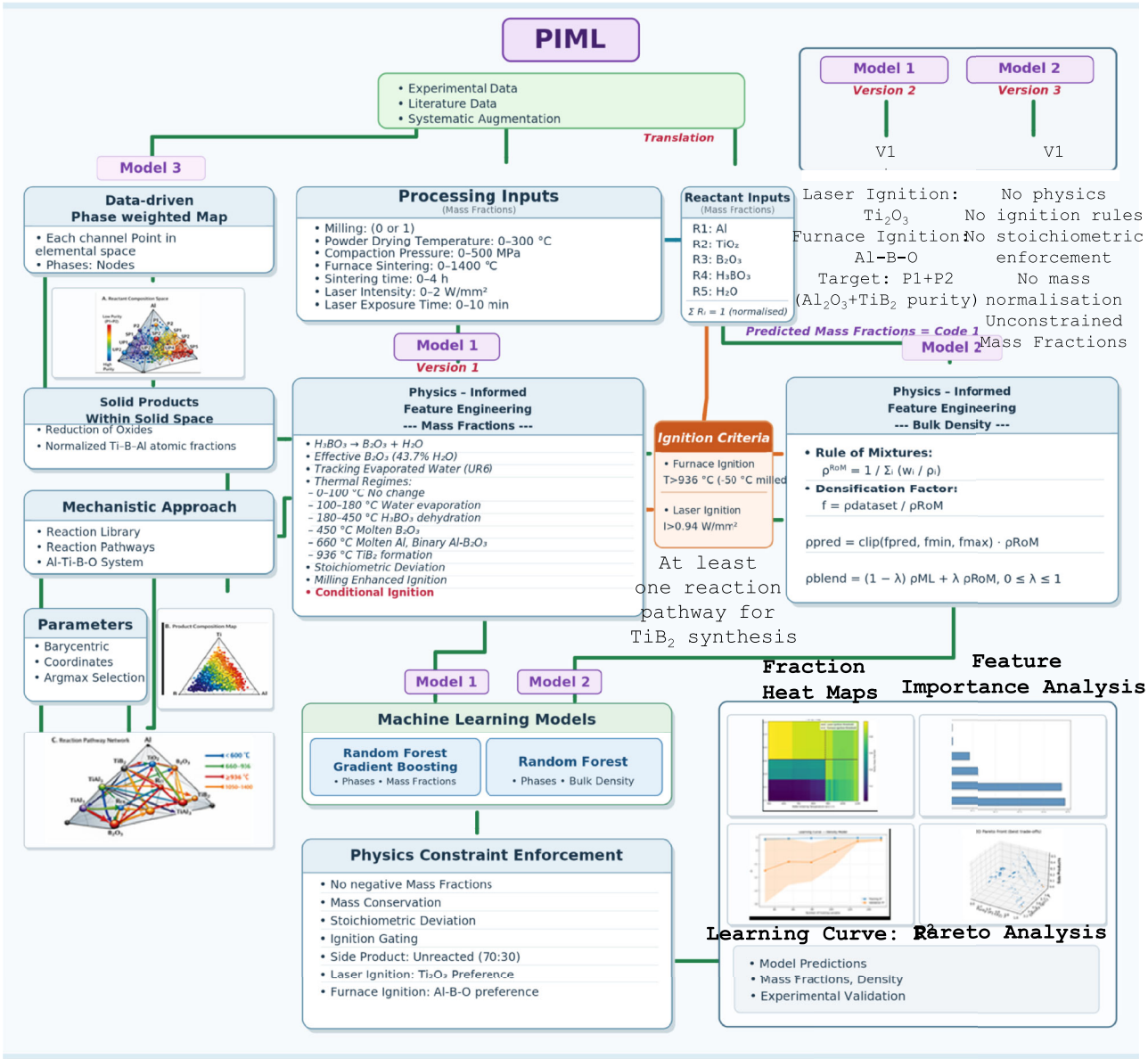


FIGURE 2 | An overview schematic of the PIML model, which integrates Model 1 for physics-informed mass-fraction prediction, Model 2 for bulk-density prediction, and Model 3 for generating a data-driven phase-weighted map, solid-products ternary map, and a mechanistic approach to reaction pathways in barycentric coordinates.

0.993 testing hold-out accuracy. V3 frequently produced non-physical outputs: (i) negative phase fractions, (ii) compositions that deviated from 1, and (iii) unrealistic interpolation across distinct reaction regimes.

The test hold-out accuracy of the bulk density model was 0.927 (MAE: 0.1188 and RSME: 0.1382) (Table 10). The 5-fold cross-validation R^2 was reported as 0.920 ± 0.041.

The learning curve analysis (Figure 4A–C) revealed convergence of the training accuracy at values above 0.994 for all versions. The V1 model revealed poor early-stage validation, with validation R^2 values remaining negative for 60% of the dataset and converging to 0.483 by the completion of the dataset. Version 2 demonstrated improved stability and faster validation convergence, with validation R^2 values exceeding 0.98. Version 3 showed poor learning curve performance, with a validation R^2 of 0.209. The learning curve analysis of the bulk density prediction model (Figure 4D) presented convergence of training accuracy at 0.959 and achieved a validation performance of 0.898.

3.2 | Feature Importance and Physical Interpretability

Permutation-based feature importance analysis was performed for the mass fraction (V1, V2, and V3) and bulk density models (Figure 5). Reactants were excluded from the analysis to identify the impact of each processing parameter on the mass fraction of the composites. When all processing parameters were considered (Figure 5A), laser intensity during ignition (W/mm^2) was the dominant driving force for achieving high-purity products, exceeding the influence of all other processing variables by more than an order of magnitude. After excluding laser

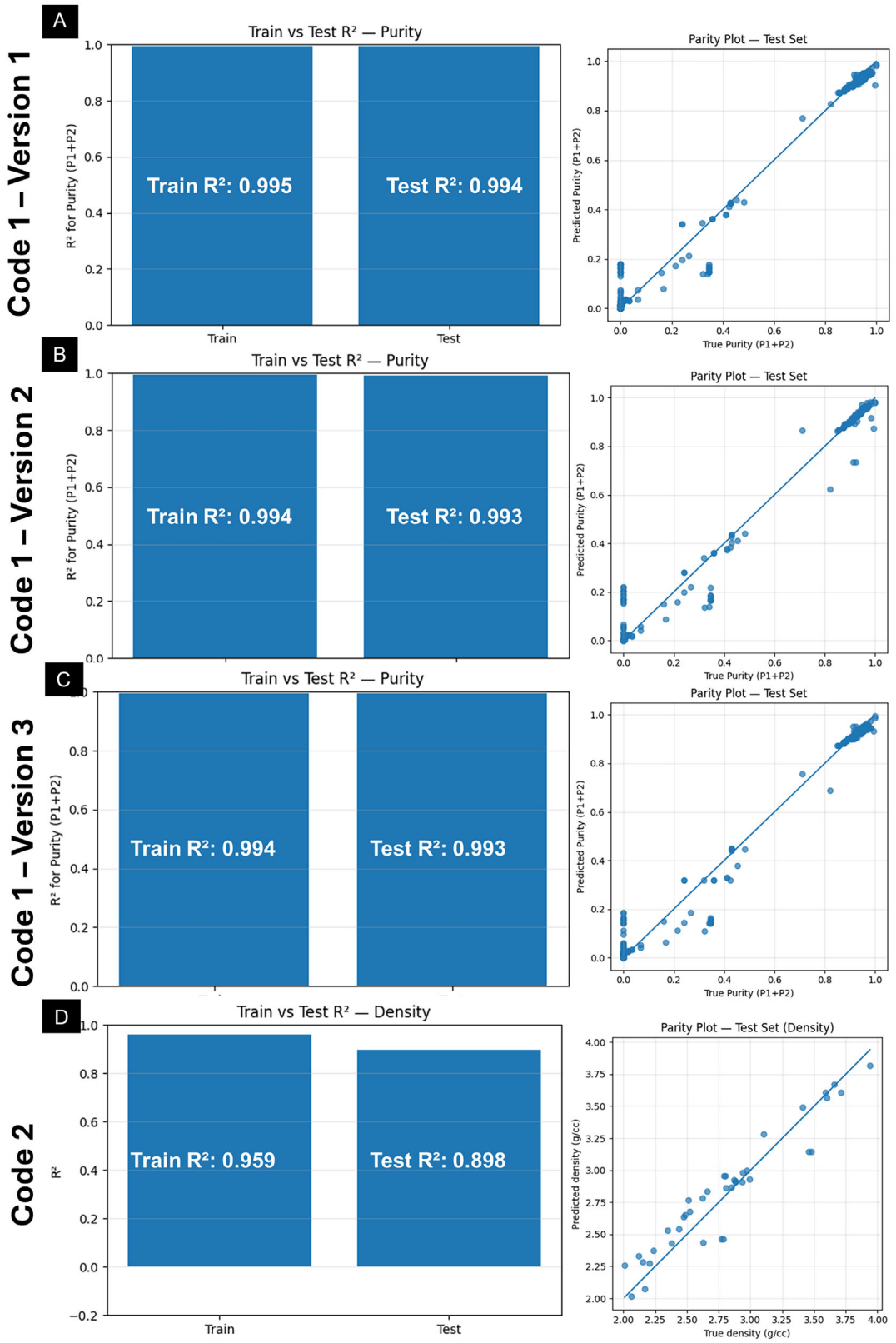


FIGURE 3 | The hold-out accuracy and parity plots for Model 1—V1, V2, and V3 and Model 2.

intensity used for ignition (W/mm^2) (Figure 5B), laser sintering time (min) (0.49) and laser sintering intensity (W/mm^2) (0.47) emerged as the dominant contributors to high-purity products, followed by furnace sintering time (h) and powder drying temperature (°C).

Permutation-based feature importance analysis for the bulk density model (Figure 5C,D) showed that milling (0.738) and laser intensity during ignition (W/mm^2) (0.547) were the most significant aspects for achieving high-density products. Random Forest intrinsic importance analysis demonstrated the reverse effect,

TABLE 9 | The hold-out, 5-fold cross validation, and learning curve analysis of the V1, V2, and V3 mass fraction prediction models.

		Random Forest			Gradient Boosting		
Option	**Metric**	**Train**	**Test**	**MAE**	**Train**	**Test**	**MAE**
V1	Hold-out	0.995	0.994	0.0035	0.994	0.993	0.0035
	5-fold cross-validation R^2	0.989 ± 0.002		0.0187 ± 0.0014	0.993 ± 0.001		0.0139 ± 0.0007
	Learning curve	0.995	0.483	—	0.995	0.486	—
V2	Hold-out	0.994	0.993	0.0162	0.994	0.993	0.0035
	5-fold cross-validation R^2	0.989 ± 0.002		0.0187 ± 0.0014	0.993 ± 0.001		0.0139 ± 0.0007
	Learning curve	0.994	0.993	—	0.994	0.993	—
V3	Hold-out	0.994	0.993	—	0.994	0.993	—
	5-fold cross-validation R^2	0.989 ± 0.002		0.0185 ± 0.0013	0.992 ± 0.001		0.0138 ± 0.0009
	Learning curve	0.994	0.131	—	0.994	0.993	—

TABLE 10 | The hold-out, 5-fold cross validation, and learning curve analysis of the bulk density prediction model.

	Random Forest			
Metric	**Train R^2**	**Test R^2**	**MAE, g/cc**	**RSME, g/cc**
Hold-out	0.952	0.927	0.1188	0.1382
5-fold cross-validation R^2	0.920 ± 0.041		0.1088 ± 0.0196	—
Learning curve	0.961	0.898	—	—

with laser intensity during ignition (W/mm^2) (0.5) being more influential than milling for producing a high-density composite. The difference between the two permutation results stems from the bias of tree-based intrinsic metrics toward variables with higher variance or stronger early splits.

3.3 | Phase Fraction Maps

The phase fraction maps (Figure 6) for V1, V2, and V3 exhibited the predicted product purity as a function of laser intensity (W/mm^2) and furnace sintering temperature (°C). For V1 and V2, Figure 6A features sharp transitions from reactants to products, which aligned with the ignition thresholds in the Al–TiO_2–B_2O_3–H_3BO_3 system by Daskalakis et al. [14]. In Figure 6B, the model predicted a low (but nonzero) presence of the Al_2O_3 phase below the ignition thresholds, deriving from the Al–B_2O_3 binary system, consistent with the imposed reaction constraints. The highest purity composite (Al_2O_3 0.79 wt%–TiB_2 0.21 wt.%) was predicted for pellet sintering between 500 and 600 °C, followed by laser ignition at 0.94 W/mm^2. The TiB_2 formation onset was predicted for laser intensities greater than 0.94 W/mm^2 and furnace sintering temperatures greater than 884 °C (Figure 6B). In the case of V3 (Figure 6D–F), where no physic constraints were introduced, products formed for laser intensities greater than 0.44 W/mm^2, while phase purity was improved for furnace sintering temperature above 936 °C (Figure 6G). The heatmaps for Model 2 demonstrated that furnace sintering above 450 °C (melting of B_2O_3) and cold pressing of reactants between 175–375 MPa improved the bulk density of the composites (Figure 6H). Milling the reactants, using low laser intensity for LIChemS, and heat treating the reactants to dissolve H_3BO_3 optimized bulk density (Figure 6I).

3.4 | Case Study: Physics-Informed ML Model and Pure ML Model

The first case study compared predictions from V1, V2, and V3 for phase fractions and density under identical LIChemS processing conditions for (i) stoichiometric, (ii) nonstoichiometric, and (iii) conditional stoichiometric compositions and no ignition scenario (Table 11).

For LIChemS stoichiometric ignition (Option 1—Table 1), V1 and V2 predicted P1(Al_2O_3) = 0.6584 and P2(TiB_2) = 0.3386, which yielded a product purity of 0.9970. No unreacted phases (UR1–UR4) were present in the final product due to the nature of stoichiometric ignition. The mass fraction of the side-products remained below 0.003. All physics-informed predictions remained non-negative and satisfied mass conservation.

For nonstoichiometric ignition (Option 2—Table 1), V1 and V2 predicted P1 = 0.7122 and P2 = 0.2671, adding up to a product purity of 0.9793, with the mass fraction of SP1(Ti_2O_3) being 0.0125. Version 3 (pure ML) predicted P1 (Al_2O_3) as 0.6549, and P2 as 0.3315 and SP1 inflates to 0.3300 for (Option 1—Table 1). Negative mass fractions (SP1 = −0.0005, SP3 = −0.0002) were

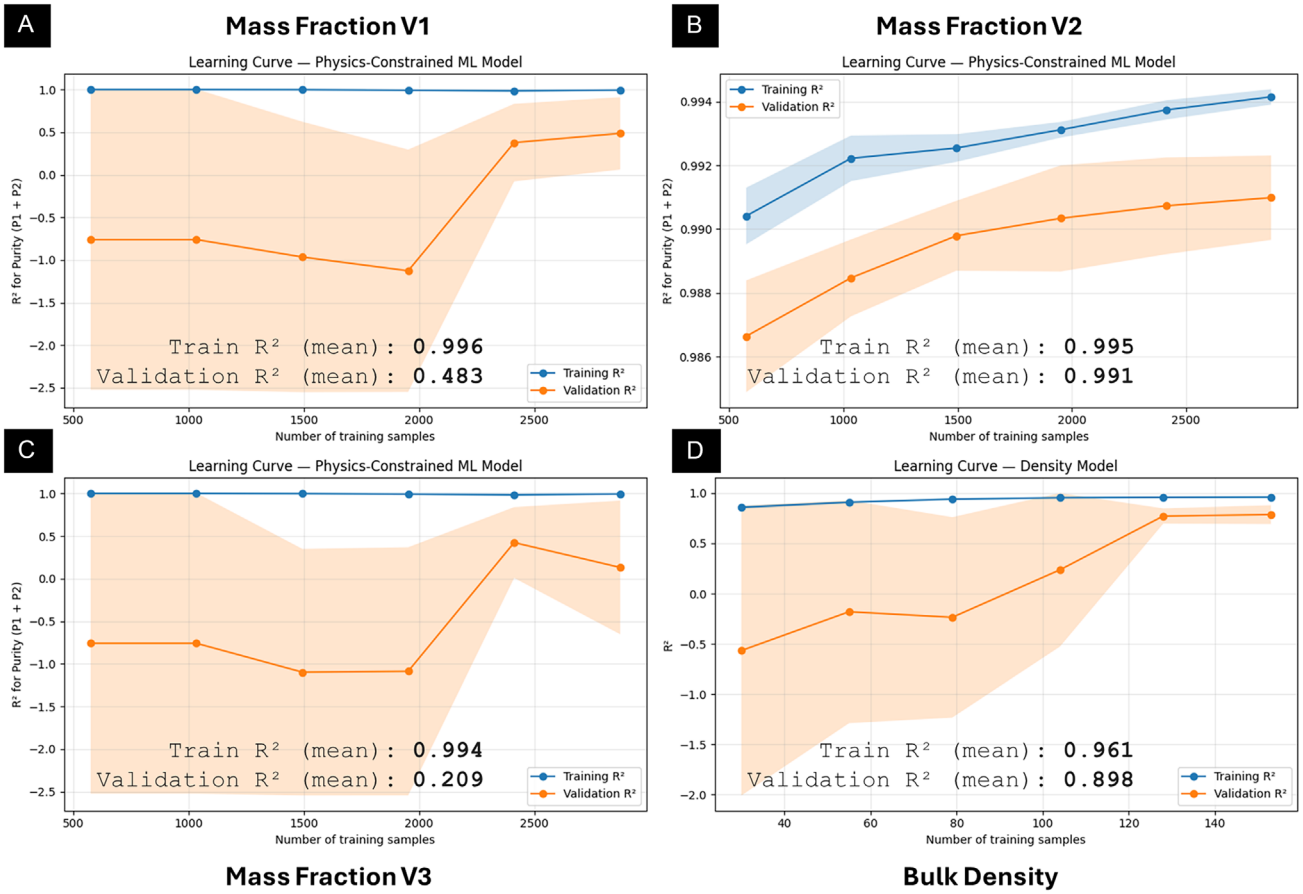


FIGURE 4 | Learning curve of the physics-informed: (A) mass fraction prediction model V1, (B) mass fraction prediction model V2, (C) mass fraction prediction model V3, and (D) bulk density prediction model.

predicted for the Al_3Ti and Al_5BO_9 phases, respectively, showcasing the absence of the non-negativity enforcement, while the total mass added up to 1.0286. For the nonstoichiometric composition (Option 2—Table 1), V3 predicted P1 = 0.7066 and P2 = 0.2792.

For (Option 3—Table 1), the contrast was more pronounced, as V1 predicted P1 = 0.6618 and P2 = 0.3341 (purity = 0.9959).The concentration of unreacted material was negligible. V3 predicted large leftover reactant mass fractions (UR1 = 0.3246, UR2 = 0.2645) and high product mass fractions (P1 = 0.6626, P2 = 0.3236), violating mass conservation.

Under no-ignition conditions, V1 and V2 predicted that no P1 and P2 were formed and the mass fraction of the reactants remained high (UR1 = 0.3462, UR2 = 0.2880, UR3 = 0.3180). The V1 and V2 models predicted that a small amount of Ti_2O_3 and Al_5BO_9 phases formed. Version 3 predicted product formation (P1 = 0.6709, P2 = 0.2334) despite the processing parameters not exceeding the ignition threshold.

The ML predicted bulk density for (Option 1—Table 1) was 3.84 g/cc, while the RoM baseline deriving from the mass fraction of the predicted phases was 4.14 g/cc, and the blended density output was 3.86 g/cc, with MAE 0.035 g/cc and RMSE 0.042 g/cc. For (Option 2—Table 1), the deviation (MAE 0.1188 g/cc) was higher. Then, in (Option 3—Table 1), MAE was 0.061 g/cc. The largest deviation between RoM (2.93 g/cc) and ML (3.78 g/cc)-predicted bulk densities was observed in the case of no ignition (Table 12).

3.5 | Case Study: Physics-Informed ML Model and Experimental Data

The predicted mass fractions (Model 1—V1, V2) and predicted bulk density (Model 2) were compared to Al2O3–TiB2 composites experimentally synthesized through LIChemS. The LIChemS composite mainly consisted of P1 (Al_2O_3 0.69) and P2 (TiB_2) 0.22, yielding a combined product purity of 0.91. V1 predicted P1 = 0.7016 and P2 = 0.2300 (purity = 0.9316), while V2 predicted P1 = 0.7164 and P2 = 0.2307 (purity = 0.9471). Both physics-informed models slightly overestimated product purity and presented a slight deviation of (4%) from experimental measurements. The measured SP1 (Ti_2O_3) was 0.06, while V1 and V2 predicted SP1 = 0.0459 and 0.0467, respectively, possibly due to the ignition-gated constraint integrated into the models, which favored the formation of Al_2O_3 and TiB_2 phases for stoichiometric conditions and limited the formation of Ti_2O_3. The X-ray diffractograms of the experimentally synthesized composite showed no reactant phases (UR1–UR4), while V1 and V2 predicted minor concentrations (Supporting Information S3.1). The predicted bulk density of the composite by Model 2 (3.68 g/cc) was comparable to the experimental density of 3.71 g/cc. The Rule-of-Mixtures density (RoM) was 4.01 g/cc, greater than the experimental density by

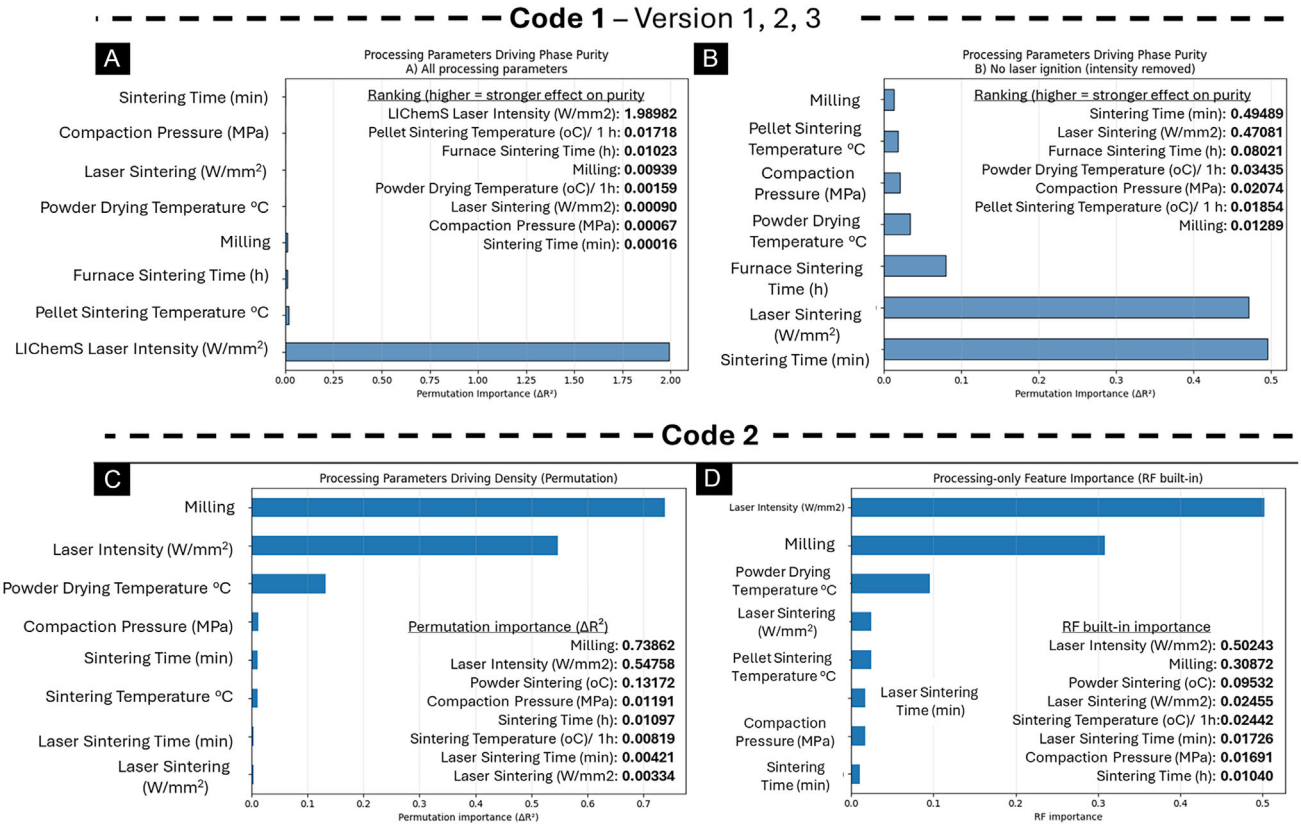


FIGURE 5 | Physics-informed feature importance analysis on the effect of processing inputs on the purity of the produced composite. (A) Permutation importance analysis of phase purity when including all processing parameters. (B) Permutation importance analysis of phase purity when excluding the laser ignition parameter (W/mm^2). (C) Permutation importance analysis of bulk density when including all processing parameters. (D) Random Forest importance analysis of bulk density when including all processing parameters.

0.30 g/cc. This was attributed to the model assuming ideal packing and no porosity.

3.6 | Pareto Analysis

The 3-objective Pareto analysis was performed on 800 processing combinations to achieve (P1 + P2> 0.85), bulk density (>3.5 g/cc), and suppressed the mass fractions of side-products (<0.1). Figure 7 shows the Pareto fronts for V1, V2, and V3. The V1 identified 3 Pareto-optimal solutions (Table 13), located within a narrow processing window defined by pellet sintering temperatures of 501–586 °C, laser intensities of 0.97–1.14 W/mm^2, compaction pressures ranging from 110 to 452 MPa, furnace sintering times between 0.86 and 2.24 h, and powder drying temperatures of 300–374 °C. All Pareto-optimal points were predicted above the boric acid decomposition temperature threshold, and they clustered around the laser ignition threshold (~0.94 W/mm^2). Dehydration kinetics and reactions, rather than arbitrary parameter combinations, defined the optimal tradeoffs. The narrow geometry of the Pareto front (Figure 7A) described the thermochemical regimes imposed by the physics constraints.

For V2 (Figure 7B and Table 13), three Pareto-optimal solutions were identified within a tightly bounded processing window achieved through processing parameters that involve pellet sintering temperatures of 502–592 °C, laser intensities of 0.97–1.12 W/mm^2, compaction pressures of 270–452 MPa, furnace sintering times of 0.44–2.24 h, and powder drying temperatures of 252–356 °C. Compared to V1, the Pareto region in V2 exhibited stronger clustering for higher compaction pressures and ignition-threshold laser intensities, improving the suppression of thermodynamically inconsistent pathways.

The purely machine-learning model (V3) produced five Pareto-optimal solutions with a less structured front (Figure 7C and Table 13). Most solutions exhibited a broader variation in the compaction pressure parameter and less clustering of solutions around the ignition threshold. V3 also showed greater variation in density and side-product formation, as it could not discriminate similar to V1 and V2 between physically viable and non-viable outputs.

3.7 | Compositional Topology and Product-Space Mapping of the Outputs

Figure 8A presents a frequency-weighted phase dominance map inside the Al–B–Ti–O tetrahedral composition space, utilizing the 3800 predicted phase outputs from the dataset. Each node corresponded to a specific phase centroid positioned according to its normalized atomic fractions (Equation (25)). The nodes indicated the frequency that each phase was present across the dataset. The dominant predicted phases were P1 (Al_2O_3,

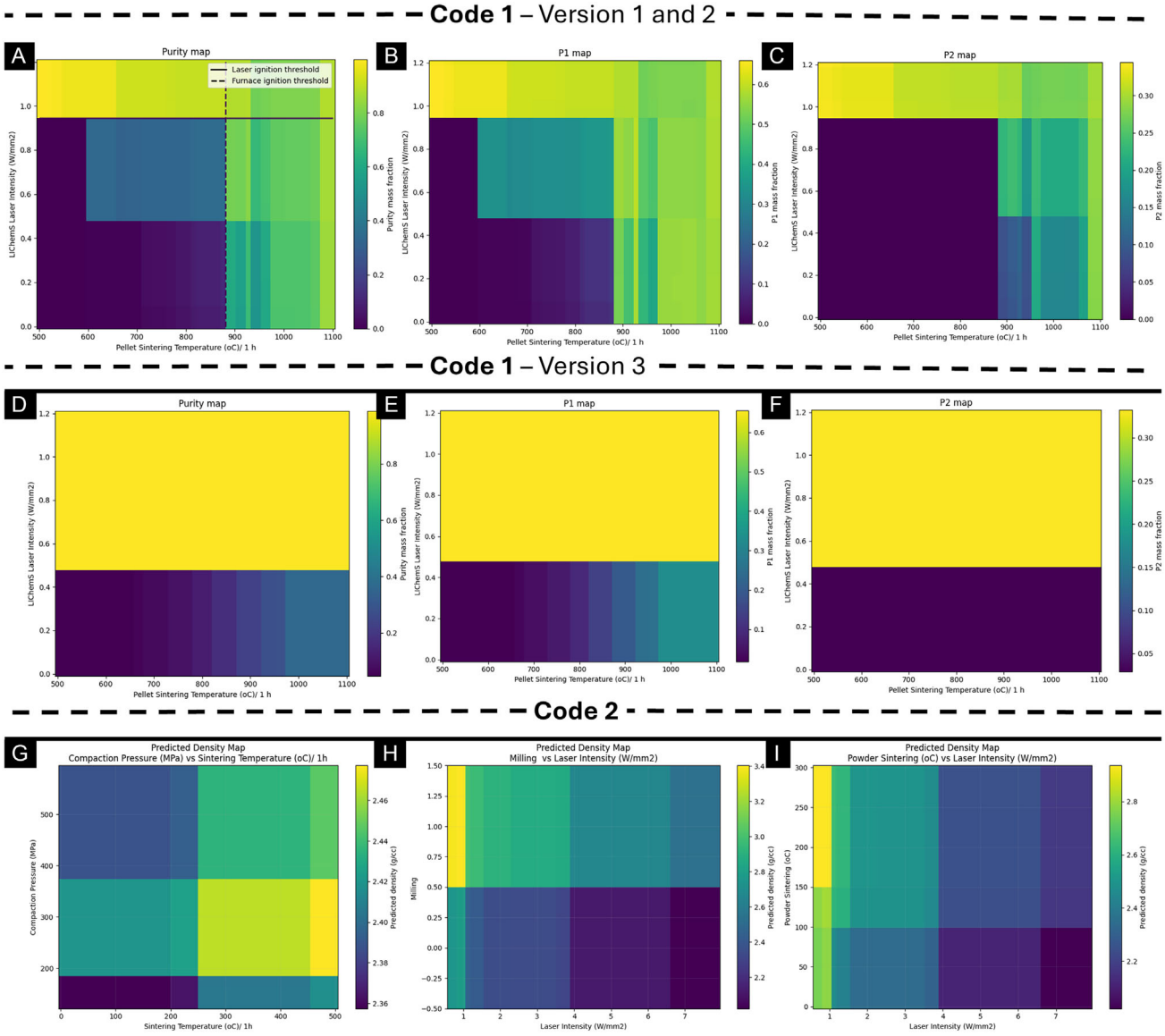


FIGURE 6 | Predicted phase mass fractions and bulk density of Al_2O_3–TiB_2 composites synthesised from the Al–TiO_2–B_2O_3–H_3BO_3 reactive system as a function of processing parameters. (A–C) Physics-informed Model 1 (V1/V2) predictions of (A) combined Al_2O_3–TiB_2 phase purity (P1 + P2), (B) Al_2O_3 mass fraction (P1), and (C) TiB_2 mass fraction (P2), as functions of pellet sintering temperature (°C) and LIChemS laser intensity (W/mm²). (D–F) Corresponding predictions from the unconstrained machine-learning model (V3), showing (D) combined phase purity, (E) Al_2O_3 mass fraction, and (F) TiB_2 mass fraction under the same processing conditions. (G–I) Model 2 predictions of composite bulk density (g/cm³) as functions of (G) pellet sintering temperature and compaction pressure, (H) mechanical milling and laser intensity, and (I) powder sintering temperature and laser intensity. The maps illustrate the influence of ignition thresholds, thermochemical processing conditions, and mechanical activation on phase formation and composite densification.

$n = 1672$) and P2 (TiB_2, $n = 986$). They clustered close to the O-rich and Ti-rich regions of the tetrahedron, respectively, which is consistent with the outputs of the aluminothermic reduction of B_2O_3 and TiO_2. Unreacted phases (UP1–UP4) were positioned closer to the edges, which were incomplete ignition regimes. Side products SP1 (Ti_2O_3, $n = 965$) and SP2 ($TiAl_3$, $n = 44$) occupied the space between the reactant and product (Equation (16)–(21)). The relatively low frequencies of the aluminoborate phases (SP3, SP4) were consistent with the lack of furnace-dominant reactions (Equations (22)–(24)).

Figure 8B exhibits the Ti–B–Al ternary projection of the 3800 mass-fraction outputs after reducing the oxides to their metallic constituents and normalizing their atomic fractions. The cluster of points generated within the ternary diagram shifted toward the Ti–Al side, and it corresponded to Al_2O_3–TiB_2 phase formation following SHS (Equations (21) and (22)). The products were generated as an output of 2 parameters: (i) oxidation of Al from the oxides to form Al_2O_3 and (ii) formation of TiB_2 from boron and Ti. Lower-purity outputs were aligned closer to the Al-rich edge of the ternary. These outputs corresponded to incomplete ignition or subignition threshold processing conditions. The lack of points predicted closer to the B vertex indicated that the model did not consider the accumulation of free boron but instead assumed its reaction with Al or Ti–O phases to form TiB_2 or Al–B–O intermediate phases (Equations (24)–(26)). Model 3

TABLE 11 | The predictive outputs of mass fractions based on Model 1—V1, V2, and V3.

Mass fractions	Option 1 (ignition)	Option 2 (ignition)	Option 3 (ignition)	Option 1 (no ignition)
Model 1—Version 1 (12 outputs)				
UP1	0.0000	0.0024	0.0000	0.3462
UP2	0.0000	0.0021	0.0000	0.2880
UP3	0.0000	0.0017	0.0000	0.3180
UP4	0.0000	0.0000	0.0000	0.0059
P1	0.6584	0.7122	0.6618	0.0000
P2	0.3386	0.2671	0.3341	0.0000
SP1	0.0025	0.0125	0.0035	0.0150
SP2	0.0001	0.0016	0.0001	0.0037
SP3	0.0003	0.0003	0.0004	0.0212
SP4	0.0001	0.0000	0.0002	0.0021
SP5	0.0000	0.0000	0.0000	0.0000
Model 1—Version 2 (P1+P2 purity focus)				
UP1	0.0000	0.0025	0.0000	0.3462
UP2	0.0000	0.0022	0.0000	0.2880
UP3	0.0000	0.0017	0.0000	0.3180
UP4	0.0000	0.0000	0.0000	0.0059
P1	0.6568	0.7133	0.6581	0.0000
P2	0.3402	0.2652	0.3379	0.0000
SP1	0.0000	0.0108	0.0000	0.0150
SP2	0.0001	0.0017	0.0000	0.0037
SP3	0.0021	0.0022	0.0024	0.0212
SP4	0.0008	0.0003	0.0015	0.0021
SP5	0.0000	0.0000	0.0000	0.0000
Model 1—Version 3 (no physics–pure ML)				
UP1	0.0049	0.0049	0.3246	0.0124
UP2	0.0038	0.0039	0.2645	0.0046
UP3	0.0299	0.0017	0.1231	0.0581
UP4	0.0000	0.0000	−0.0008	−0.0000
P1	0.6578	0.7066	0.6626	0.6709
P2	0.3315	0.2792	0.3236	0.2334
SP1	−0.0005	0.0034	0.0011	0.0114
SP2	0.0012	0.0012	0.0003	0.0056
SP3	−0.0002	0.0027	0.0070	0.0059
SP4	0.0002	0.0003	0.0006	0.0002
SP5	0.0000	0.0000	0.0000	0.0000

displayed realistic product outputs mainly dominated by Al_2O_3 and TiB_2 phases rather than arbitrary Ti-rich, B-rich, or Al-rich phases.

Figure 9 displays a stoichiometric–topological tetrahedral map that depicts the products and reactions during LIChemS and furnace SHS within a barycentric Al–B–Ti–O space. Each phase was positioned according to its atomic fractions. In the thermal regime below 660 °C, the reactions remained confined near oxygen-rich compositions, as limited reductions between Al and B_2O_3 took place. Within the 660–936 °C regime, the molten B_2O_3 triggered Al–B–O interactions. Above the ignition threshold (≥936 °C), a topological transition promoted the formation of Al_2O_3–TiB_2 composites. In the (1050–1400 °C) thermal regime, secondary reactions took place, producing the Al_5BO_9, $Al_{18}B_4O_{33}$, and $TiBO_3$ phases. All equations for the topological map are included in the Supporting Information S2.5.

4 | Discussion

In this work, we developed a novel PIML model by integrating thermochemical constraints into machine learning to predict the mass fractions and bulk density of Al_2O_3–TiB_2 composites synthesized in situ from the (Al–TiO_2–B_2O_3–H_3BO_3) system. Unlike purely statistical approaches, the PIML predicted ignition-controlled phase transformation with high accuracy. The PIML model provided a computationally efficient alternative to reaction–diffusion or CALPHAD-based approaches [51].

The PIML results aligned with experimental findings in the Al–TiO_2–B_2O_3 reactive system, as observed by Daskalakis et al. [14]. SHS was described by Sytschev [1] and Merzhanov [1], as a threshold-driven process, where ignition events defined phase transformation and the topology of the reactions instead of the continuous thermodynamic interpolations. The ignition-controlled behavior was constructed in this PIML model by integrating laser and furnace ignition gating mechanisms, temperature regimes, and stoichiometric enforcement rules.

Daskalakis et al. [10, 14] demonstrated experimentally that laser ignition chemical synthesis (LIChemS) at 0.94 W mm^{-2} produced sharp transitions in the composition of the products, where partially reduced intermediates were converted to TiB_2–Al_2O_3 phases. The Ti_2O_3 phase was a byproduct of the B_2O_3 deficiency in the starting stoichiometry. The PIML model developed in this work demonstrated this behavior in three independent ways (i) heat maps, (ii) feature importance analysis, and (iii) Pareto analysis. Phase fraction heatmaps exhibited a sharp transition from reactants to products past the laser intensity mark of 0.94 W mm^{-2} and furnace temperatures ≥936 °C [10].

Feature-importance analysis identified laser intensity as the main processing parameter affecting product purity, while Pareto optimization also identified solutions at ignition thresholds rather than at extreme processing conditions. This contrasts conventional CALPHAD and equilibrium thermodynamic modeling [21, 22] as they assume homogeneous equilibrium and may not capture the threshold-driven phase transformation during LIChemS.

In the literature, aluminoborate phases formed in heating regimes between 450 and 660 °C [10] and above 1050 °C [10, 14, 39]. In the present model, aluminoborate phases (SP3, SP4) primarily formed within the defined high-temperature regime (1050–1400 °C). The low concentration of $Al_{18}B_4O_{33}$ predicted in the dominance map resulted from its absence in the LIChemS dataset. Unlike purely statistical regression, the

TABLE 12 | The predictive outputs for bulk density based on Model 2.

Options	Machine learning, g/cc	Rule of mixtures ML prediction, g/cc	P blend, g/cc	MAE, g/cc	RMSE, g/cc
Option 1 ignition	3.84	4.14	3.86	0.035	0.042
Option 2 ignition	3.73	4.1	3.72	0.1188	0.1382
Option 3 ignition	3.81	4.12	3.8	0.061	0.094
Option 1 no ignition	3.78	2.93	3.51	0.1382	0.1423

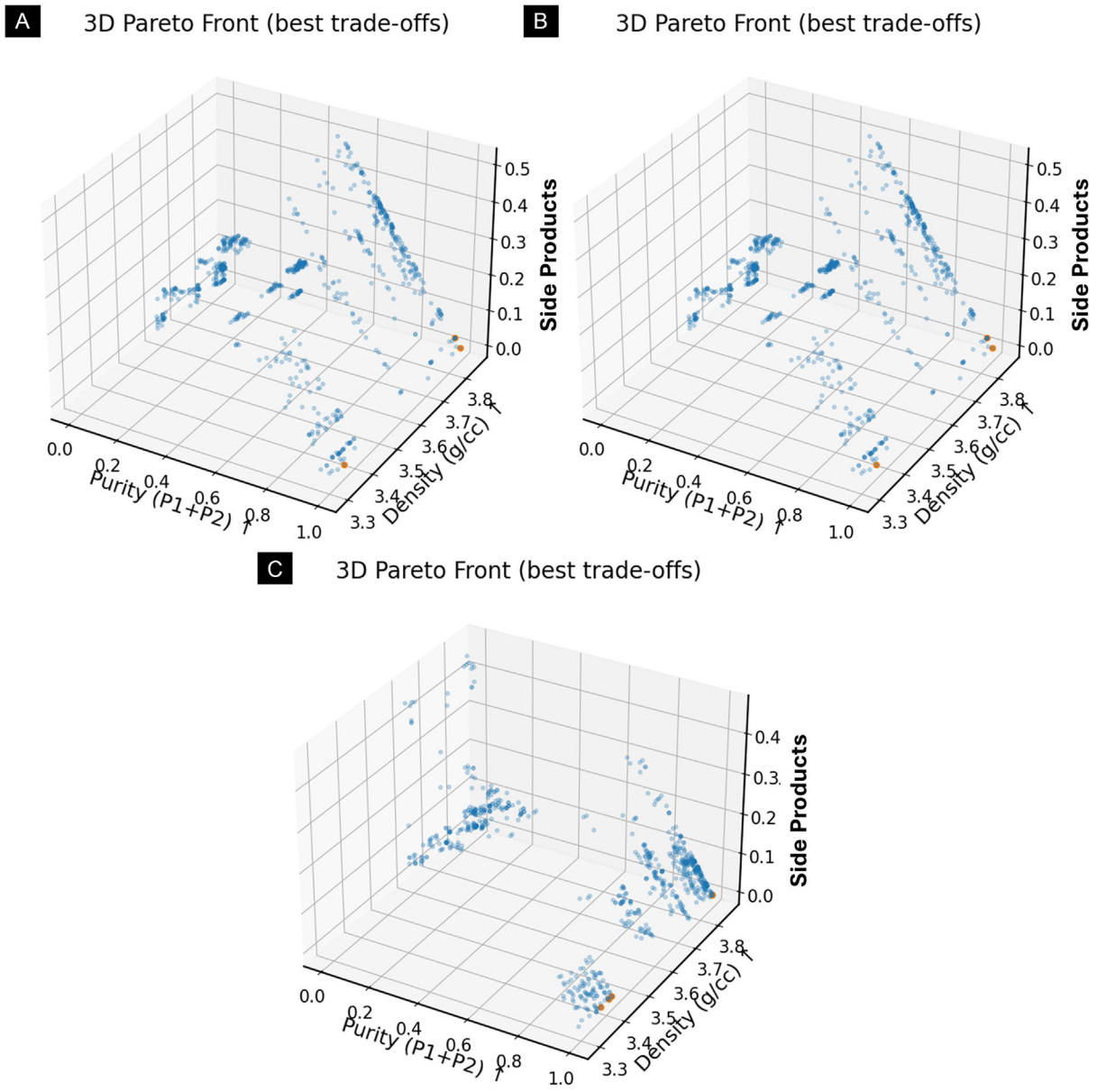


FIGURE 7 | Pareto analysis for identifying the optimal solutions when using (A) V1, (B) V2, and (C) V3.

PIML model in this work accurately matched experimentally observed outputs without introducing reaction–diffusion equations or kinetic parameters.

Data-driven models used to synthesize ceramic and energy-demanding materials have reported high predictive accuracy but often lack physical enforcement of mass conservation, non-negativity, and reaction feasibility. Unconstrained regression models in the literature were capable of interpolating outputs smoothly across discontinuous reaction regimes, leading to physically inconsistent outputs when extrapolating beyond dense data regions [37, 38].

TABLE 13 | The optimal Pareto solutions for V1, V2, and V3.

Pareto point	Pellet sintering temp, °C, 1 h	Laser intensity, W/mm^2	Compaction pressure, MP	Furnace time, h	Laser time, min	Drying temp, °C, 1h
V1						
1	502.8448	1.0240	409.5595	0.8603	7.9564	356.6475
2	501.1578	1.1435	109.9900	1.8197	7.4573	374.3798
3	586.0100	0.9723	452.4367	2.2388	4.3693	300.5483
V2						
1	501.16	1.144	109.99	1.82	7.46	374.38
2	502.84	1.024	409.56	0.86	7.96	356.65
3	586.01	0.972	452.44	2.24	4.37	300.55
V3						
1	557.8346	1.0831	327.8881	1.0089	3.7536	273.7659
2	502.8448	1.0240	409.5595	0.8603	7.9564	356.6475
3	591.7263	1.1048	270.6935	0.4379	4.0816	338.3371
4	586.0100	0.9723	452.4367	2.2388	4.3693	300.5483
5	539.1294	1.1185	350.8309	2.1391	9.2977	252.1972

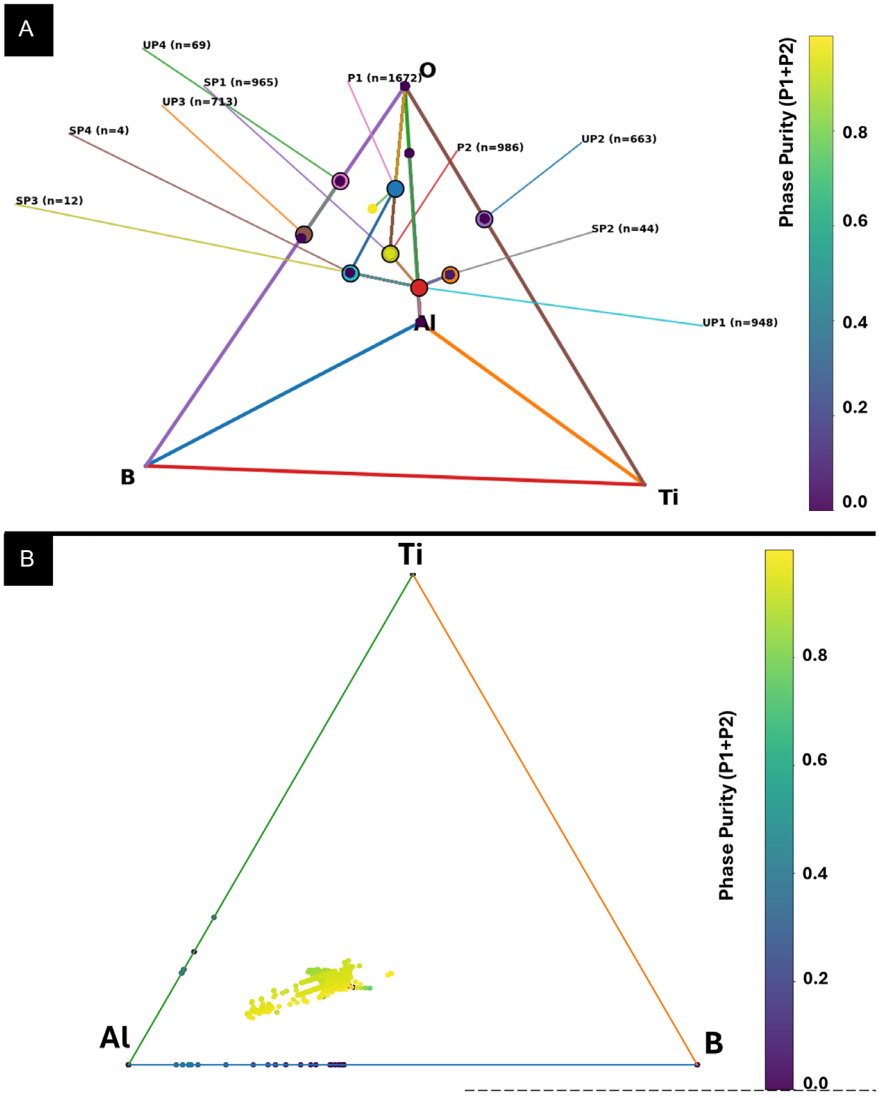


FIGURE 8 | (A) Data-driven frequency-weighted phase dominance map. (B) Solid products within the Al–Ti–B compositional space following SHS.

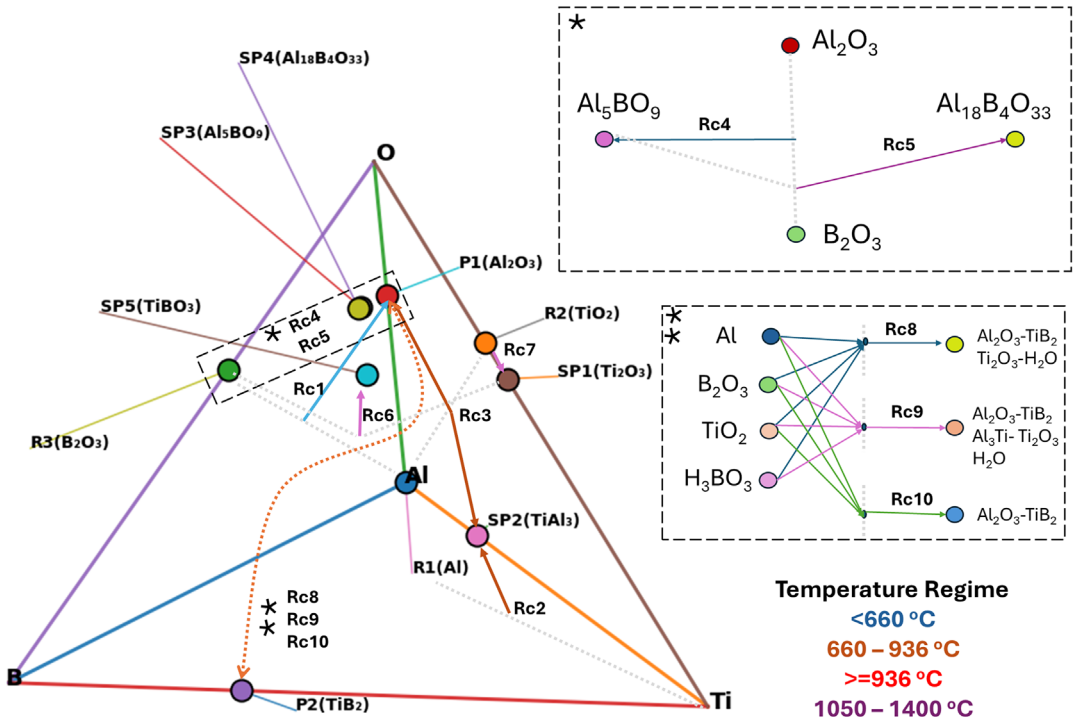


FIGURE 9 | Mechanistic tetrahedral map of the reaction pathway topology.

Numerical accuracy alone did not ensure chemical validity in the (Al–TiO_2–B_2O_3–H_3BO_3) reactive system. Although the unconstrained model (V3) achieved similar hold-out R^2 to the physics-informed V1 and V2, after removing any physics constraints such as (i) dehydration chemistry, (ii) ignition thresholds, and (iii) post-prediction constraints, it produced chemically invalid predictions including negative phase fractions, violated ($\Sigma w_i \neq 1$), and predicted product phases under nonignition conditions. The high predictive accuracy of the models was due to fixed reaction stoichiometry, the existence of ignition thresholds, and the limited competitive side phase formation at each thermal regime. The findings were consistent with results observed in ML-based materials modeling literature regarding the absence of conservation enforcement [52]. The machine learning model may not have distinguished between the laser-intensity column used to sinter the samples and the laser-intensity column describing LIChemS.

The Model 1—V1 and V2 models integrated (i) H_3BO_3 dehydration kinetics, (ii) effective B_2O_3 recalculation, (iii) ignition gating (laser and furnace), (iv) stoichiometric deviation metrics, and (v) milling parameters, which constrained the learning problem for the model and allowed only the prediction of physically permissible outputs. In V1, purity (P1+P2) was derived after (i) predicting a 12-component vector, (ii) applying clipping, (iii) renormalization, and (iv) rule-based redistribution, which amplified small errors in P1 and P2. V2 reduced the error by supervising purity as a main target, improving generalization in ignition-active regimes. The learning curve analysis, especially for V1, showed that validation was improved when SHS channels were represented (~8% of dataset) [53].

Experimental data matched PIML predictions under LIChemS conditions. V1 and V2 predictions deviated 3-4% from the composition of the experimentally synthesized composite (P1 ≈ 0.69, P2 ≈ 0.22) and slightly underestimated the composition of Ti_2O_3. Density predictions also agreed with the experimental values (3.68 vs 3.71 g/cc). The rule-of-mixtures density was calculated to be 4.01 g/cc. The greater value was attributed to the assumption by the model of ideal packing and the absence of porosity (Table 14).

During Pareto optimization, the PIML models identified a narrow feasible window for achieving (purity > 0.85, density 3.34 /cc, side products > 0.1) for laser intensity (~1 W mm^{-2}), pellet sintering temperatures (500–600 °C), and drying temperatures above (250 °C), which agrees with LIChemS-optimized parameters [14]. In contrast, V3 produced a Pareto surface displaying weaker clustering at the ignition threshold due to its inability to distinguish between viable and nonviable reaction pathways.

Compositional topology and product-space mapping demonstrated that SHS outcomes were arranged in a constrained domain instead of arbitrary Ti–B–Al combinations. The tetrahedral dominance map and ternary projection exhibited the synthesis of Al_2O_3–TiB_2-rich compositions consistent with the threshold-driven reactive system [1].

The dataset mainly consisted of literature data points, while partial systematic augmentation was performed to reduce uncertainty in the Al–B_2O_3 binary and LIChemS (unmilled, laser intensity for sintering at 0.44 W mm^{-2}) regimes. The density model did include physics constraints regarding particle size distributions, volume reduction due to SHS, and porosity due to degassing.

Our PIML models enable accurate predictive outputs without the need of extensive experimental trial-and-error in the Al–TiO_2–B_2O_3–H_3BO_3 system. It offers a pathway to reduce raw-material

TABLE 14 | Mass fractions and bulk density comparisons between Model 1—V1 and V2 and Model 2 and experimental data.

Model 1—V1		Model 1—V2		Experimental data	
Phases	**Mass fraction**	**Phases**	**Mass fraction**	**Phases**	**Mass fraction**
UR1	0.0079	UR1	0.0067	UR1	0.0000
UR2	0.0071	UR2	0.0039	UR2	0.0000
UR3	0.0055	UR3	0.0070	UR3	0.0000
UR4	0.0000	UR4	0.0000	UR4	0.0000
P1	0.7016	P1	0.7164	P1	0.69
P2	0.2300	P2	0.2307	P2	0.22
SP1	0.0459	SP1	0.0467	SP1	0.06
SP2	0.0016	SP2	0.0016	SP2	0.02
SP3	0.0004	SP3	0.0053	SP3	0.01
SP4	0.0000	SP4	0.0029	SP4	0.0000
SP5	0.0000	SP5	0.0000	SP5	0.0000
Model 2					
ML density	3.68		3.68	Density	3.71
RoM density	4.01		4.01		

waste, energy consumption, and processing time. The model can be adapted to other multicomponent oxide-reactive systems.

5 | Conclusions

In this work, we developed a novel physics-informed machine learning model for predicting the composition and bulk density of Al_2O_3–TiB_2 deriving from the exothermic Al–TiO_2–B_2O_3–H_3BO_3 reactive system. Physics-informed ML models (V1, V2) achieved testing hold-out R^2 (0.994) and ensured mass conservation and non-negative mass fractions. The unconstrained model (V3) predicted invalid outputs including negative phase fractions and the formation of the product under nonignition conditions. PIML predictions displayed (4%) deviation from the composition of the LIChemS-synthesized Al_2O_3–TiB_2 composites and (1%) deviation from the bulk density measurements. Pareto analysis identified a narrow optimal processing window for synthesizing high purity and density composites, which included (i) reactant drying temperature at 250 °C, (ii) furnace sintering temperature at 550 °C, and (iii) LIChemS at 1 W mm^{-2}. Optimal tradeoffs took place near activation thresholds rather than under extreme processing conditions. Compositional topology mapping further demonstrated that SHS did not predict arbitrary Ti–B–Al mixtures. The PIML model in this research provided high-accuracy predictions in the Al–TiO_2–B_2O_3–H_3BO_3 reactive system and can be modified to apply to other multioxide systems for real-time process monitoring and adaptive control of LIChemS manufacturing.

Acknowledgments

The authors would like to acknowledge the Defence Science and Technology Laboratory (DSTL) and UKRI PermMag-DiSARE for their financial and scientific support throughout this research. The authors also acknowledge the University of Leeds for providing the facilities for conducting the research. The authors would also like to acknowledge Chat GPT for assisting with some parts of the formatting of the Python code. Special thanks to Robert Simpson SCaPE (University of Leeds), Chris Bulman (University of Leeds), Mohamed Javed (University of Leeds), Neelam Iqbal, Tony Wiese MechEng (University of Leeds), and Camille Hammersley MechEng (University of Leeds).

Funding

This study was supported by the Defence Science and Technology Laboratory (DSTL), the Engineering and Physical Sciences Research Council (EPSRC) (1787225), and UKRI PermMag-DiSARE (10092510).

Conflicts of Interest

The authors declare no conflicts of interest.

Data Availability Statement

Data will be available upon request.

References

1. A. E. Sytschev and A. G. Merzhanov, "Self-Propagating High-Temperature Synthesis of Nanomaterials," *Russian Chemical Reviews* 73, no. 2 (2004): 147–159, https://doi.org/10.1070/RC2004v073n02ABEH000837.

2. C.-L. Yeh and K.-T. Liu, "Synthesis of TiB_2/TiC/Al_2O_3 and ZrB_2/ZrC/Al_2O_3 Composites by Low-Exotherm Thermitic Combustion With PTFE Activation," *Journal of Composites Science* 6, no. 4 (2022): 111, https://doi.org/10.3390/jcs6040111.

3. S. Roy, A. Biswas, and S. Banerjee, "Self-Propagating High-Temperature Synthesis of Titanium Borides," *Bulletin of Materials Science* 16, no. 5 (1993): 347–356, https://doi.org/10.1007/BF02759547.

4. E. A. Levashov, A. S. Mukasyan, A. S. Rogachev, and D. V. Shtansky, "Self-Propagating High-Temperature Synthesis of Advanced Materials and Coatings," *International Materials Reviews* 62, no. 4 (2016): 203–239, https://doi.org/10.1080/09506608.2016.1243291.

5. H. Sina and S. Iyengar, "Reactive Synthesis and Characterization of Titanium Aluminides Produced From Elemental Powder Mixtures,"

Journal of Thermal Analysis and Calorimetry 122, no. 2 (2015): 689–698, https://doi.org/10.1007/s10973-015-4815-6.

6. E. Hannachi, K. A. Mahmoud, M. I. Sayyed, and Y. Slimani, "Effect of Sintering Conditions on the Radiation Shielding Characteristics of YBCO Superconducting Ceramics," *Journal of Physics and Chemistry of Solids* 164 (2022): 110627, https://doi.org/10.1016/j.jpcs.2022.110627.

7. P. Mossino, "Some Aspects in Self-Propagating High-Temperature Synthesis," *Ceramics International* 30, no. 3 (2004): 311–332, https://doi.org/10.1016/S0272-8842(03)00119-6.

8. N. A. Kochetov and A. Sychev, "Effect of SiO_2 Content and Mechanical Activation on Ni–Al–SiO_2 Combustion," *Combustion, Explosion, and Shock Waves* 56, no. 5 (2020): 520–526.

9. Y. Yuan, X. Liu, Y. Tu, et al., "Characterization of Interface Properties and Enhancement of Thermal Hardness in TiN/(CrVTaTiW)Nx Multilayered Structures: Investigating Diverse Crystallization Templates," *Journal of Alloys and Compounds* 1020 (2025): 179440, https://doi.org/10.1016/j.jallcom.2025.179440.

10. E. Daskalakis, A. Scott, and A. Jha, "Enhancing the Ignitability of the Al–TiO_2–B_2O_3 Powder Mixture Through Intensive Vibratory Ball Milling (C: P12)," *Ceramics International* 49 (2023): 24142–24155.

11. F. Mao, Z. Chang, X. Zhang, and Q. Yan, "SiC Ceramics Strengthened and Toughened With a Crystallized Intergranular Phase Network Structure," *Journal of the European Ceramic Society* 44, no. 7 (2024): 4350–4361, https://doi.org/10.1016/j.jeurceramsoc.2024.01.049.

12. X. Liu, Y. Chen, L. Li, et al., "Understanding the Growth Mechanisms of TiO_2/Al_2O_3 Mixed Scales Formed on Al-Depleted Ti_2AlC at 1000–1200 °C," *Corrosion Science* 204 (2022): 110393, https://doi.org/10.1016/j.corsci.2022.110393.

13. M. Vlasova, M. Kakazey, M. Aguilar, et al., "Directed Laser Processing of Compacted Powder Mixtures Al_2O_3-TiO_2-Y_2O_3," *Science of Sintering* 45, no. 3 (2013): 247–259, https://doi.org/10.2298/SOS1303247V.

14. E. Daskalakis, A. Scott, R. Mangham, N. Middleton, and A. Jha, "Laser Ignition Chemical Synthesis of Bulk Al_2O_3-TiB_2 Composites for Impact Resistance Application," *Journal of Materials Research and Technology* 38 (2025): 6063–6082, https://doi.org/10.1016/j.jmrt.2025.09.045.

15. E. M. Sharifi, F. Karimzadeh, and M. H. Enayati, "Preparation of Al_2O_3–TiB_2 Nanocomposite Powder by Mechanochemical Reaction Between Al, B_2O_3 and Ti," *Advanced Powder Technology* 22, no. 4 (2011): 526–531.

16. Y. Jaluria, *Advanced Materials Processing and Manufacturing*, (Springer, 2018).

17. N. Kochetov, "Combustion and Characteristics of Mechanically Activated Ni+ Al Mixture: Effects of the Weight and Size of the Milling Balls," *Russian Journal of Physical Chemistry B* 10, no. 4 (2016): 639–643, https://doi.org/10.1134/S1990793116040047.

18. T. M. Vidyuk, M. A. Korchagin, D. V. Dudina, and B. B. Bokhonov, "Synthesis of Ceramic and Composite Materials Using a Combination of Self-Propagating High-Temperature Synthesis and Spark Plasma Sintering," *Combustion, Explosion, and Shock Waves* 57, no. 4 (2021): 385–397.

19. A. Kroupa, "Modelling of Phase Diagrams and Thermodynamic Properties Using Calphad Method–Development of Thermodynamic Databases," *Computational Materials Science* 66 (2013): 3–13, https://doi.org/10.1016/j.commatsci.2012.02.003.

20. G. Inden, *Ordered Intermetallics—Physical Metallurgy and Mechanical Behaviour*, (Springer, 1992), 89–91.

21. N. Saunders and A. P. Miodownik, *CALPHAD (Calculation of Phase Diagrams): A Comprehensive Guide. Vol. 1*, (Elsevier, 1998).

22. L. Yonghe, Y. Sheng, Z. Weijing, and L. Hoyi, "Thermodynamic Analysis of the Self-Propagation High-Temperature Synthesis Al_2O_3/B_4C Composite," *Scripta Materialia* 39, no. 9 (1998): 1237–1242, https://doi.org/10.1016/S1359-6462(98)00304-2.

23. M. R. Andalibi, P. Bowen, A. Carino, and A. Testino, "Global Uncertainty-Sensitivity Analysis on Mechanistic Kinetic Models: From Model Assessment to Theory-Driven Design of Nanoparticles," *Computers & Chemical Engineering* 140 (2020): 106971, https://doi.org/10.1016/j.compchemeng.2020.106971.

24. H. Zhou, A. Lu, C. Zheng, Y. Wang, X. Kong, and W. Wu, "Experimental and Numerical Approach of Afterburning Effects in Fuel-Rich Explosives Within Confined Spaces," *Defence Technology* 51 (2025): 67–79, https://doi.org/10.1016/j.dt.2025.05.009.

25. T. J. Snee, C. Bassani, and J. A. M. Ligthart, "Determination of the Thermokinetic Parameters of an Exothermic Reaction Using Isothermal, Adiabatic and Temperature-Programmed Calorimetry in Conjunction With Spectrophotometry," *Journal of Loss Prevention in the Process Industries* 6, no. 2 (1993): 87–94, https://doi.org/10.1016/0950-4230(93)90005-I.

26. T. Zhou, Z. Song, and K. Sundmacher, "Big Data Creates New Opportunities for Materials Research: A Review on Methods and Applications of Machine Learning for Materials Design," *Engineering* 5, no. 6 (2019): 1017–1026, https://doi.org/10.1016/j.eng.2019.02.011.

27. G. Huang, Y. Guo, Y. Chen, and Z. Nie, "Application of Machine Learning in Material Synthesis and Property Prediction," *Materials* 16, no. 17 (2023): 5977, https://doi.org/10.3390/ma16175977.

28. M. A. Mellal, *Artificial Intelligence in Material Science*, (CRC Press, 2024), 208–234.

29. X.-H. Zhu and Y. Zhang, "Functional Applications and Data-Driven Design of High-Entropy Ceramics," *High Entropy Alloys & Materials* 2, no. 2 (2024): 219–245, https://doi.org/10.1007/s44210-024-00046-y.

30. J. Krzywanski, M. Sosnowski, K. Grabowska, A. Zylka, L. Lasek, and A. Kijo-Kleczkowska, "Advanced Computational Methods for Modeling, Prediction and Optimization—A Review," *Materials* 17, no. 14 (2024): 3521, https://doi.org/10.3390/ma17143521.

31. K. Sattari, "Physics-Informed Data-Driven Frameworks for Materials Discovery," (Doctoral dissertation, University of Missouri-Columbia, 2024).

32. J. Mousa, "Physically Consistent Hybrid Modeling for Chemical Process Systems via Neural Networks and Data Reconciliation," (Doctoral dissertation, Université de Toulouse, 2025).

33. M. Ahmadi, D. Biswas, M. Lin, F. D. Vrionis, J. Hashemi, and Y. Tang, "Physics-Informed Machine Learning for Advancing Computational Medical Imaging: Integrating Data-Driven Approaches With Fundamental Physical Principles," *Artificial Intelligence Review* 58, no. 10 (2025): 297, https://doi.org/10.1007/s10462-025-11303-w.

34. G. Sharma, S. Loganathan, E. Daskalakis, E. K. Barimah, S. Strafford, and A. Jha, "Phase Stability in Rare-Earth-Doped Apatites: A Machine Learning Approach," *Advanced Intelligent Systems* 7, no. 11 (2025): 2500293.

35. G. Sharma, S. Loganathan, E. K. Barimah, et al., "Effect of Rare Earth Ion Substitution on Phase Decomposition of Apatite Structure," *ChemPhysChem* 25, no. 19 (2024): e202400109.

36. C. Meng, S. Griesemer, D. Cao, S. Seo, and Y. Liu, "When Physics Meets Machine Learning: A Survey of Physics-Informed Machine Learning," *Machine Learning for Computational Science and Engineering* 1, no. 1 (2025): 20, https://doi.org/10.1007/s44379-025-00016-0.

37. G. E. Karniadakis, I. G. Kevrekidis, L. Lu, P. Perdikaris, S. Wang, and L. Yang, "Physics-Informed Machine Learning," *Nature Reviews Physics* 3, no. 6 (2021): 422–440, https://doi.org/10.1038/s42254-021-00314-5.

38. J. Willard, X. Jia, S. Xu, and M. Steinbach, Integrating Physics-Based Modeling With Machine Learning: A Survey, 1, 1, 2020, 1–34, arXiv preprint arXiv:2003.04919

39. V. Sundaram, K. Logan, and R. Speyer, "Aluminothermic Reaction Path in the Synthesis of a $TiB_2Al_2O_3$ Composite," *Journal of Materials*

Research 12, no. 7 (1997): 1681–1684, https://doi.org/10.1557/JMR.1997.0230.

40. Z. Y. Ma and S. C. Tjong, "In Situ Ceramic Particle-Reinforced Aluminum Matrix Composites Fabricated by Reaction Pressing in the TiO_2 (Ti)-Al-B (B_2O_3) Systems," *Metallurgical and Materials Transactions A* 28, no. 9 (1997): 1931–1942, https://doi.org/10.1007/s11661-997-0123-5.

41. M. A. Meyers, E. A. Olevsky, J. Ma, and M. Jamet, "Combustion Synthesis/Densification of an Al_2O_3–TiB_2 Composite," *Materials Science and Engineering: A* 311, no. 1 (2001): 83–99, https://doi.org/10.1016/S0921-5093(01)00930-3.

42. K. Logan, J. Sparrow, and W. McLemore, *Combustion and plasma synthesis of high-temperature materials*, (VCH Publishers, 1990), 219–228.

43. NIST, 2002, Sintered Alumina (Al_2O_3).

44. NIST, 2002, Titanium Diboride (TiB_2).

45. NIST, 2026, Aluminum.

46. NIST, Rutile TiO_2, 2026.

47. NIST, Diboron Trioxide, 2026.

48. NIST, Aluminum borate, 2026.

49. B. Özgür, O. Bilaç, and C. Duran, "Synthesis of Aluminum Borate Powder, Fabrication and Characterization of Aluminum Borate-Based Ceramics," *Ceramics International* 50, no. 9 (2024): 14987–14995.

50. M. Fisch, T. Armbruster, D. Rentsch, E. Libowitzky, and T. Pettke, "Crystal-Chemistry of Mullite-Type Aluminoborates $Al_{18}B_4O_{33}$ and Al_5BO_9: A Stoichiometry Puzzle," *Journal of Solid State Chemistry* 184, no. 1 (2011): 70–80, https://doi.org/10.1016/j.jssc.2010.10.032.

51. Z.-K. Liu, *Zentropy*, (Jenny Stanford Publishing, 2024), 273–348, https://doi.org/10.1201/9781032692401.

52. M. R. Flickinger, S. Raguraman, A. L. Polk, et al., "Machine Learning-Assisted Analysis of Ignition and Combustion Properties in as-Milled and Annealed Al-Zr Composite Powders," *Combustion and Flame* 284 (2026): 114660, https://doi.org/10.1016/j.combustflame.2025.114660.

53. N. Alampara, A. Aneesh, Mño Ríos-García, et al., "General-Purpose Models for the Chemical Sciences: LLMs and Beyond," *Chemical Reviews* 126 (2026): 2484, https://doi.org/10.1021/acs.chemrev.5c00583.

Supporting Information

Additional supporting information can be found online in the Supporting Information section.